ICAS 2021 SHANGHAI
International Council of the Aeronautical Sciences
32nd Congress of the International Council of the Aeronautical Sciences
September 6-10, 2021
Pudong Shangri-La, Shanghai, China

STATIC AEROELASTIC COMPUTATIONS OF WING CONFIGURATIONS IN TRANSONIC FLOWS AT HIGH REYNOLDS NUMBERS

J Allan A. Lyrio[1], João Luiz F. Azevedo[2], Domingos A. Rade[1] & Ricardo G. da Silva[2]

[1]Instituto Tecnológico de Aeronáutica, DCTA/ITA, São José dos Campos, SP, Brazil
[2]Instituto de Aeronáutica e Espaço, DCTA/IAE/ALA, São José dos Campos, SP, Brazil

Abstract

The present work has the objective of presenting recent developments of a static aeroelastic computational process for the analysis of typical aircraft configurations in transonic flows. The analysis procedure is assessed through the study of static aeroelastic characteristics of the HIRENASD model, which is a test cases with extensive experimental database for validation of computational results. The in-house BRU3D computational fluid dynamics (CFD) solver, which uses the fully turbulent compressible Reynolds-averaged Navier-Stokes (RANS) equations, is combined with a finite element method (FEM) modal basis code through the uses of radial basis functions (RBF) for smooth volume grid movements. Results in terms of structural displacements have shown good agreement with experimental data, although indicating that further grid refinement for the fluid domain is still necessary in order to improve the correlation of the aerodynamic coefficients.

Keywords: Static Aeroelasticity, Computational Fluid Dynamics, Radial Basis Functions, Modal Basis

1. Introduction

According to Ref. [1], the objectives of the High Reynolds Number Aerostructural Dynamics project (HIRENASD) were to improve the aero-structural dynamics understanding and knowledge in the transonic regime at Reynolds numbers characteristic of real transport aircraft, and to gather experimental data in a wide range of Reynolds numbers and aerodynamic loads for current and future aeroelastic research. Although the complete results of this project are not publicly open, there are several important scientific papers along the last decades providing comparisons between experimental and computational data in terms of structural and aerodynamic fields for this configuration [2, 3, 4, 5, 6]. These references present frameworks for fluid-structure interaction (FSI) simulations and prediction of aerodynamic effects associated with wing deformation. The available experimental data cover a wide range of Reynolds numbers and dynamic pressures, thus enabling the verification and/or validation of computational FSI results, as performed in the present work.

The main objective of the research effort that led to the present work was to develop an in-house framework for static aeroelastic analyses in the transonic regime. There are three major components that form such a framework. The aerodynamic and structural dynamic analysis modules are two of such components, and a suitable procedure for communicating data from one module to the other is the third relevant component. In this context, a key enabling aspect of a robust fluid-structure coupling process is the availability of an adequate CFD volumetric mesh deformation methodology. It is clear that the CFD meshes that will afford the correct resolution of the relevant aerodynamic phenomena present in the flow will typically have a very large number of grid nodes. Moreover, such nodes are mainly concentrated near the wall, with very small spacing at the wall and stretched 3-D cells for appropriate turbulent boundary layer representation. Therefore, the requirements for moving, or deforming, such grids are quite stringent.

In the present work, the radial basis function (RBF) approach is used for such mesh motions. RBFs are widely used in the literature for mesh morphing and their formulation has been improved along the last two decades in order to deal with more refined CFD meshes [7, 8, 9, 10, 11]. In the present

case, the formulations presented in these references are implemented in our in-house framework using a parallel numerical approach that takes advantage of OpenMP calls in Fortran. The present paper does include some results that have helped define several numerical aspects associated to the use of RBFs. However, the interested reader is also referred to Ref. [12] for a more thorough analysis of the several numerical parameters required to appropriately use the RBF concept for the applications of interest to the present authors.
The material included in the paper is structured such that the process of FSI analysis is detailed described. Hence, the aerodynamic and the structural dynamic formulations are presented, as well as the details of the HIRENASD model. The process of coupling those modules, as well as the use of the RBF approach for mesh displacement, are also discussed, indicating the relevant aspects that should be taken care of for successful coupled simulations. Applications that demonstrate the quality of the analyses which are possible with the capability implemented are also included, by comparing the results obtained with the present numerical framework to the available HIRENASD experimental data.

2. Theoretical and Numerical Formulation

2.1 Aerodynamic Formulation

The BRU3D CFD code [13, 14] has been widely used at Instituto de Aeronáutica e Espaço (IAE) for aerospace simulations at high Reynolds numbers and, also, at high Mach numbers. References [15] and [16] describe the successful efforts for BRU3D validation in pure aerodynamic problems using the ONERA-M6 and DLR-F6 transonic test cases and the JAXA Standard Model (JSM) high-lift subsonic configuration. The fluid dynamics formulation present in the BRU3D code is described in Ref. [14]. It is based on the 3-D compressible Reynolds-averaged Navier-Stokes (RANS) equations, that filter the fluctuating part of the fluid properties, treated via turbulence models, and maintain only the mean contribution of the flow. These equations are also presented in Ref. [15] in their dimensional form as

$$\frac{\partial \mathbf{Q}}{\partial t} + \nabla.(\mathbf{E}_e - \mathbf{E}_v) = 0 \ , \tag{1}$$

in which $\mathbf{Q}$ is given by

$$\mathbf{Q} = [\rho \ \rho u \ \rho v \ \rho w \ e \ \rho\tau_1 \ \rho\tau_2]^T \ . \tag{2}$$

Here, ρ is the density, u, v, w are the velocity vector components, e is the total energy per unit volume and p is the static pressure. Moreover, $\mathbf{E}_e$ and $\mathbf{E}_v$ are, respectively, the inviscid and viscous flux vectors:

$$\mathbf{E}_e = \begin{bmatrix} \rho\mathbf{v} \\ (\rho u\mathbf{v} + p\hat{i}_x) \\ (\rho v\mathbf{v} + p\hat{i}_y) \\ (\rho w\mathbf{v} + p\hat{i}_z) \\ (e+p)\mathbf{v} \\ \tau_1\mathbf{v} \\ \tau_2\mathbf{v} \end{bmatrix} \ , \ \mathbf{E}_v = \begin{bmatrix} 0 \\ (\tau^l_{xi} + \tau^t_{xi})\hat{i}_i \\ (\tau^l_{yi} + \tau^t_{yi})\hat{i}_i \\ (\tau^l_{zi} + \tau^t_{zi})\hat{i}_i \\ (\beta^l_i + \beta^t_i)\hat{i}_i \\ \mu_{diff_1}\tau_{1,i}\hat{i}_i \\ \mu_{diff_2}\tau_{2,i}\hat{i}_i \end{bmatrix} \ , \tag{3}$$

with

$$\beta_i = \tau_{ij}u_j - q_{Hi} \ . \tag{4}$$

In the previous equations, the dynamic viscosity coefficient from the shear stress tensor is determined via Sutherland's formula. As also indicated in Ref. [6], the code solves the equations in an unstructured, cell-centered, conservative finite-volume formulation and advective terms are computed using the 2nd-order Roe upwind scheme.

2.2 Structural Formulation

The system of equations governing the linear dynamic structure response can be obtained through the Hamilton Principle which, according to Ref. [17], states that

$$\int_{t_1}^{t_2} (\delta L + \delta W)dt = 0 \qquad \text{, where} \qquad L = T - V \ . \tag{5}$$

In the previous equations, L is the Lagrangian function and W is the work of non-conservative forces. Associating Hamilton's Principle with the finite element discretization of the structural domain, the equations of motion are obtained in the form

$$\mathbf{M}\ddot{\mathbf{U}}(t) + \mathbf{C}\dot{\mathbf{U}}(t) + \mathbf{K}\mathbf{U}(t) = \mathbf{R}(t) \ , \tag{6}$$

where **M** is the mass matrix, **C** is the viscous damping matrix, **K** is the stiffness matrix, $\mathbf{U}(t)$ is the vector of generalized displacements, and $\mathbf{R}(t)$ is the vector of generalized forces. When dynamic effects are neglected, Eq. (6) can be reduced to a static equilibrium equation of the form

$$\mathbf{K}\mathbf{U} = \mathbf{R} \ . \tag{7}$$

In order to perform the modal projection, the eigensolutions of the associated undamped structure are first computed by solving the following eigenvalue problem:

$$(\mathbf{K} - \omega_i^2 \mathbf{M})\phi_i = \mathbf{0} \ , \tag{8}$$

where ω_i are the natural frequencies and ϕ_i denote the corresponding natural vibration modes. The displacement field is, then, expressed as a linear combination of the vibration mode shapes as

$$\mathbf{U} = \sum_{i=1}^{n} q_i \phi_i = \Phi \mathbf{q} \ . \tag{9}$$

Associating Eqs. (7) and (9), and making use of the orthogonality properties of the eigenvectors, one obtains the following solution for the reduced problem

$$\mathbf{q} = \Lambda^{-1} \Phi^T \mathbf{R} \ , \tag{10}$$

where $\Lambda = diag\{\omega_1^2 ... \omega_n^2\}$ is the spectral matrix and $\Phi = [\phi_1 ... \phi_n]$ is the modal matrix. Therefore, the static structural problem becomes dependent on the natural frequencies and associated modal shapes. Moreover, the resulting aerodynamic forces on the wing surface elements of the aerodynamic mesh are projected into the modes of the structural mesh in order to form the **R** vector.

2.3 The HIRENASD Model

The fluid dynamic domain used in the present work is discretized with the block-structured hexahedral grid, with quadrilateral surface mesh, shown in Fig. 1. The figure shows both the body and wing surfaces and the symmetry plane representations, in Fig. 1a, and a slice of the volumetric grid, in Fig. 1b. The present flow solver, however, treats the mesh as fully unstructured. Both CFD General

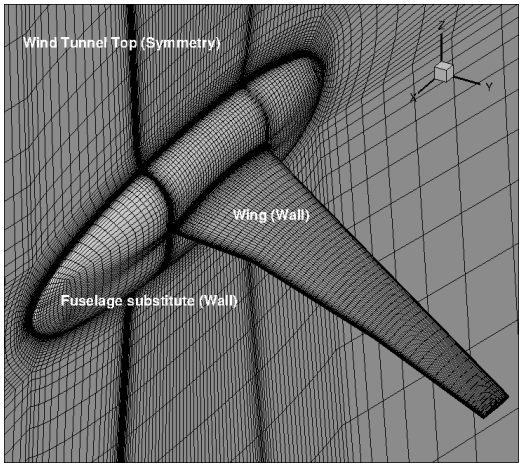

(a) Body surface and symmetry plane.

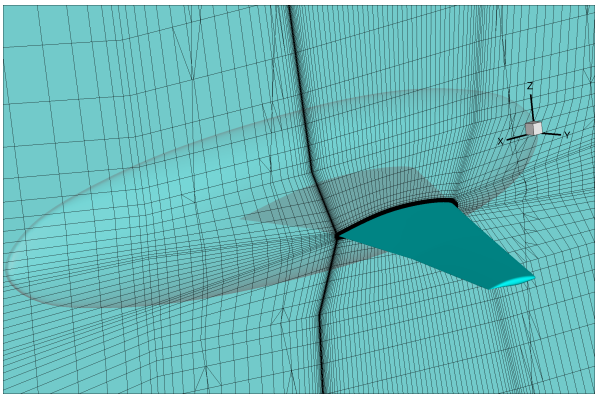

(b) Volumetric grid slice detail.

Figure 1 – Visualization of the HIRENASD aerodynamic CFD hexahedral mesh.

Notation System (CGNS) and blocking data were made available by ANSYS Germany for the 1st

AIAA Aeroelastic Prediction Workshop (AePW-1) [5]. These AePW-1 grids are refined enough to achieve the required boundary layer discretization with $Y^+ \leq 1$, according to the Reynolds number range tested in the European Transonic Wind Tunnel (ETW). However, in order to evaluate the morphing mesh capability, only the grid level 1, with 3×10^6 elements, was considered and the test further reduced the boundary layer wall resolution from 4×10^{-7} to 2×10^{-5} for the first element off the wall.
The structural domain is also provided by AePW-1 [5] consisting in a FEM unstructured tetrahedral grid, shown in Fig. 2 as a solid model. The structural model comprises the wing, the excitation transmission system and the clamping flange for the main balance connection. The FEM model has approximately 1×10^5 tetrahedral elements discretized with quadratic shape functions.

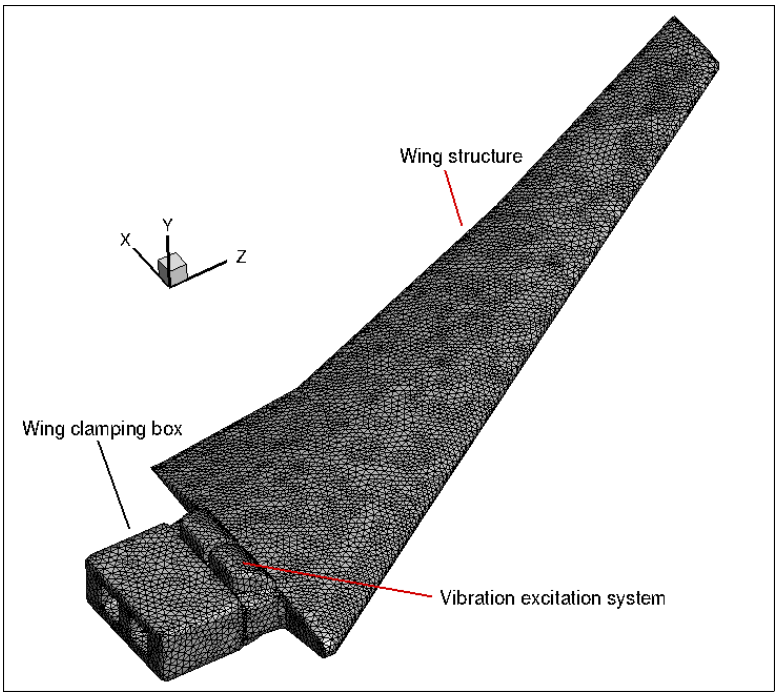

Figure 2 – HIRENASD structural solid model and visualization of surface mesh representation.

A linear modal base was obtained from the approximately 1×10^4 wing surface mesh nodes using the MSC NASTRAN solver. The wing clamping box, the vibration excitation system and the main balance were not considered for mesh morphing due to the highly rigid properties and location inside the body fuselage. A study of wing tip convergence for a given load as a function of the number of mode shapes was present in Ref. [12], with the results indicating that the use of the first 10 flexible mode shapes for the HIRENASD model was considered acceptable for a static aeroelastic simulation.

2.4 The Static Aeroelastic Process

Figure 3 shows a schematic flowchart of the implemented modal-based static aeroelastic process, in which a previous BRU3D CFD solution should be provided to accelerate the FSI process and to have an aerodynamic rigid reference solution for the rigid configuration aerodynamic loads. With the aerodynamic loads generated in the BRU3D code simulations, in terms of pressure distributions, each pressure area loads are transferred to the finite element model nearest node preserving the integral of the forces and using the Constant Strain Triangle (CST) shape function formulation [19]. A gradual loading schedule is used to avoid deflection overshoot and excessive FSI iterations.
The loads transferred to the surface FEM degrees of freedom are, then, provided to the modal based structural module developed in FORTRAN, that is capable of using the modal response results, in terms of eigenvectors and eigenvalues, in order to calculate static structural deflections. This method is specially interesting due to the fact that it eliminates full CSM solver execution. A typical wing deflection over positive aerodynamic vertical loading is shown in Fig. 4, where the bending deflection, shown in Fig. 4a, induces a local spanwise wing twist reduction and, as a consequence, the loading near to the wing tip also reduces. The wing twist distribution is shown in Fig. 4b.

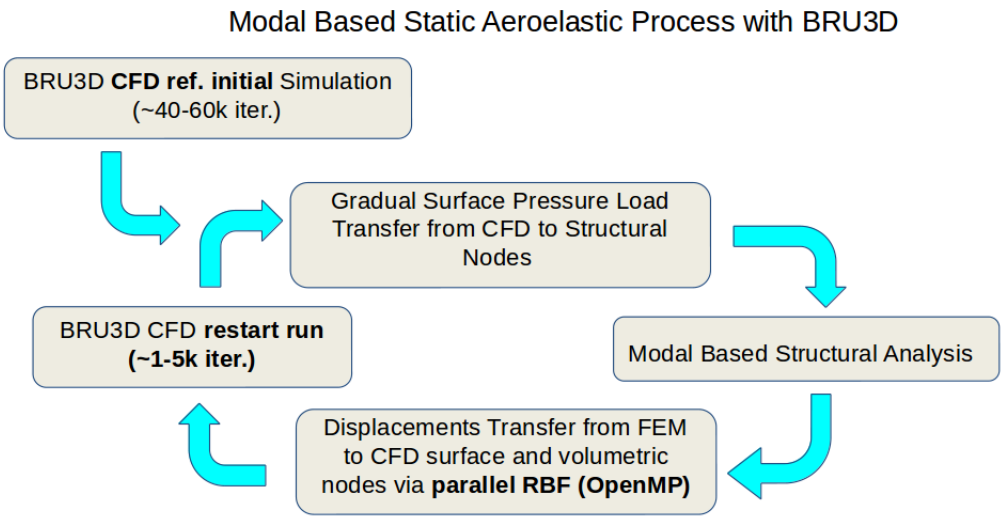

Figure 3 – The implemented static aeroelastic iterative processes using BRU3D as the CFD solver.

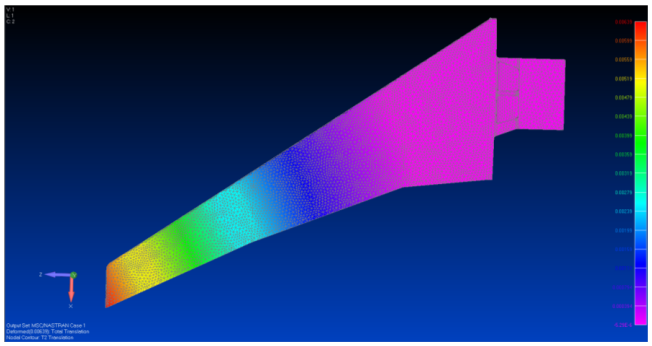

(a) Wing out-of-plane deflection field shown by isosurfaces of z-displacement.

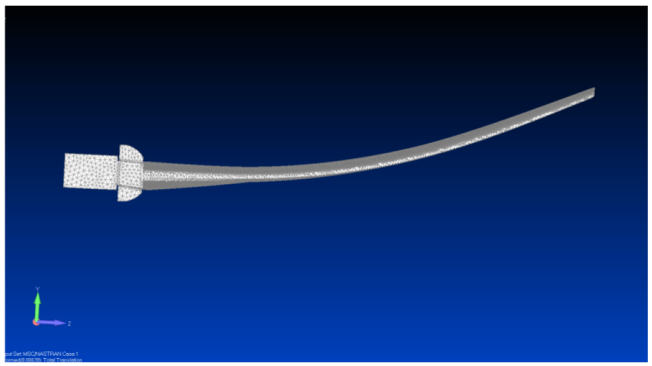

(b) Amplified swept wing twist induced by the vertical deflection.

Figure 4 – The HIRENASD structural model typical deflections.

Hence, the wing displacements are extract from finite element modal basis in proper transfer mesh nodes and, then, provided to the fluid mesh morphing process by imposing the deflected shape upon the wing. It is important to mention that fuselage, symmetry plane and far field nodes are considered to have zero deflection during the Radial Basis Function (RBF) solution system.

The RBF function used here is the Wendland C2 function [7], and some examples of such functions are shown in Fig. 5. The influence of a single function is maximum at its origin, as depicted in Fig. 5a, and the affected region depends on the so called support radius (R_{sup}) and intensity (α) to calculate this range, as it can be seen in Figs. 5b to 5e, where different combinations of these parameters lead to very different summations, represented by the $WC2_T$ curve. Thus, in order to describe a given

spatial discrete data, each RBF function must have specific intensity, *e.g.*, in Fig. 5f, for a predefined support radius. Details related to the choice of R_{sup} are described in Ref. [12].

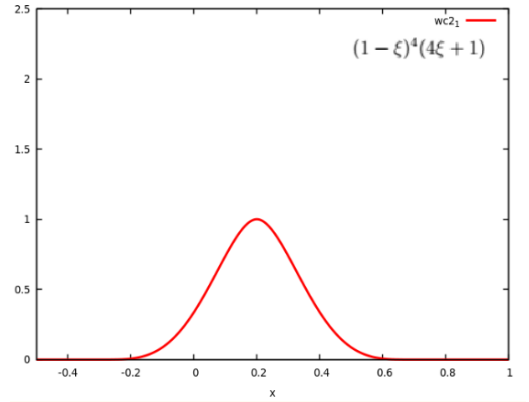

(a) $R_{sup} = 0.50,\ \alpha_i = 1.00.$

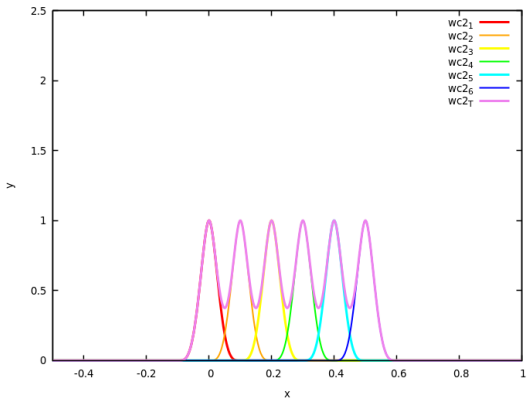

(b) $R_{sup} = 0.30,\ \alpha_i = 1.00.$

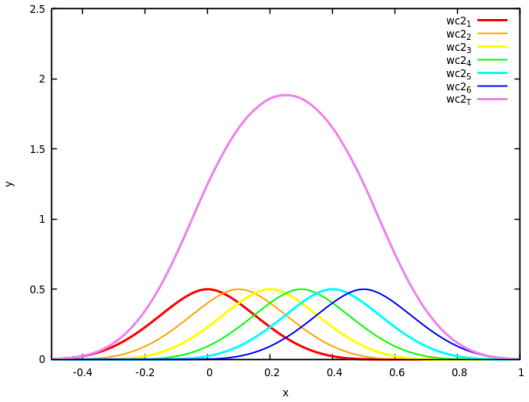

(c) $R_{sup} = 0.60,\ \alpha_i = 0.50.$

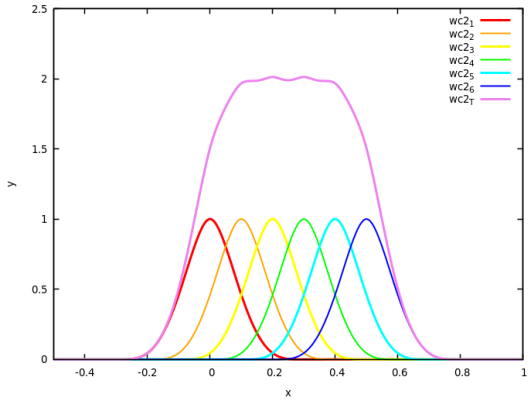

(d) $R_{sup} = 0.30,\ \alpha_i = 1.00.$

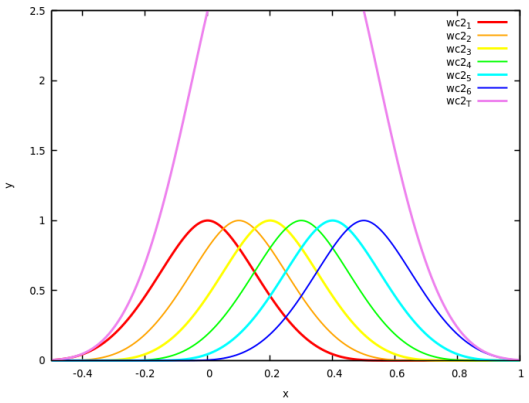

(e) $R_{sup} = 0.60,\ \alpha_i = 1.00.$

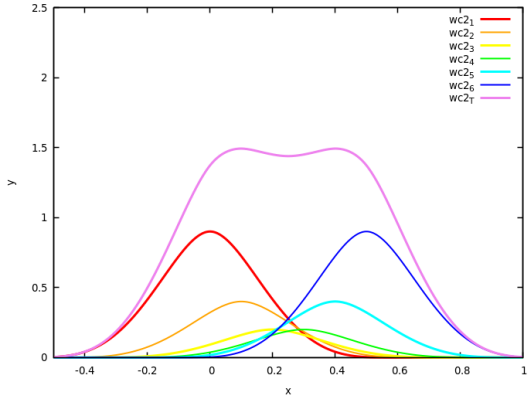

(f) $R_{sup} = 0.60,$
$\alpha_i = [0.90, 0.40, 0.20, 0.20, 0.40, 0.90].$

Figure 5 – The Wendland RBF C2 summation examples.

Radial basis functions are widely used for multivariable interpolation. In the present work, a RBF-based numerical FORTRAN in-house code for fluid mesh morphing was developed based on the material presented in Refs. [7, 8, 9], where a node displacement calculated during the structural analysis can be approximated by a sum of basis functions as

$$d_i(x) = \sum_{j=1}^{Nb} \alpha_j \phi(||x - x_{bj}||) + p_t(x)\ . \tag{11}$$

Moreover, the system of equations for RBF calculation has to be defined in three directions, *i.e.*, $\mathbf{d}_i(x) = [\Delta\mathbf{x}, \Delta\mathbf{y}, \Delta\mathbf{z}]$, for the calculation of the α_x, α_y and α_z coefficients. Therefore, three linear systems

of equations are solved using the GMRES method [20]. After this first stage of calculations, the volume mesh, indicated by the v subscript, is updated using the aero-structural **A** matrix as

$$\Delta \mathbf{x}_v = \mathbf{A}\alpha_x \ . \tag{12}$$

The same procedure is performed for the y and z directions.

3. Results

According to Ref. [1], the HIRENASD model was tested in ETW wind tunnel varying the following parameters: Mach number, Reynolds number, angle of attack, and dynamic pressure over Young's modulus. In the present work, the flow conditions used for both rigid and aerostructural computations are restricted to the ETW series 1 tests, which are shown in Table 1. The main focus here is on process validation and, hence, the selection of these conditions. Moreover, some of the HIRENASD project results are not publicly open. The computational results from the present investigation are compared to the experimental data available in Refs. [2, 4] in terms of wing bending and spanwise twist, and lift and pitching moment integrated coefficients. Furthermore, field pressure coefficient distributions evidence the effect of wing loading reduction due to flexibility deflections.

Table 1 – HIRENASD static aeroelastic conditions to be simulated in the present work based on $C_{ref} = 0.3445$ m and $b_{ref} = 1.250$ m, according to Ref. [5].

ETW Series	Re [-]	q/E$\times 10^6$ [-]	Mach number [-]	Angle of attack [deg]
1	7×10^6	0.22	0.80	0.5
1	7×10^6	0.22	0.80	1.5
1	7×10^6	0.22	0.80	2.5

3.1 Wing Deflection

Figures 6 and 7 present the converged wing bending deflection and wing spanwise twist for the three angles of attack listed in Table 1. These results are compared to experimental wing tip data from Refs. [2] and [4], represented by the horizontal black lines in both plots for each angle of attack. Although some relatively small deviations are found for the wing tip displacement at $\alpha = 0.5\ deg$ and $\alpha = 1.5\ deg$, the overall overall agreement of the present computational results is quite good.
Even for the present relatively low normalized dynamic pressure value of $q/E = 0.22 \times 10^{-6}$, the coupling between wing deflection and twist for the HIRENASD model can be noticed. The wing tip deflection between 10 and 20 mm produces a wing tip angle of attack reduction near 0.50 deg., which is relevant from an aerodynamic point of view. This effect will certainly increase with higher q/E values. In addition, the increase in wing tip z-displacement and twist, in the experimental data, with the angle of attack variation, appears to be linear, indicating that the use of a FEM modal-based approach is valid for this wind tunnel model steel structure, at least at the moderate flow condition here addressed.

3.2 Aerodynamic Coefficients

As reported in Ref. [12], the global aerodynamic coefficient changes are caused mainly by the reduction of the spanwise local angles of attack due to the coupling between bending and twist when the wing is loaded. Here, a comparison of the global lift and pitching moment coefficients, C_L and C_M, is performed. Figure 8a shows that the present static aeroelastic results for C_L, in red circles, agree with the experimental European Transonic Windtunnel (ETW) data from Ref. [2]. The rigid aerodynamic results computed with the same CFD solver, in blue squares, are also shown in the figure. It is clear that the inclusion of wing deflection in the computational results has an effect in the agreement with the experimental data. The pitching moment comparisons are presented in Fig. 8b. In this case, the agreement between the present aerostructural calculations and the experimental data is not as clear. One can observe, however, that the inclusion of structural flexibility in the C_M calculations is consistently reducing the magnitude of the pitching moment, as expected. However, it seems that the slope of the C_M curve, as a function of angle of attack, is rather different for the computational

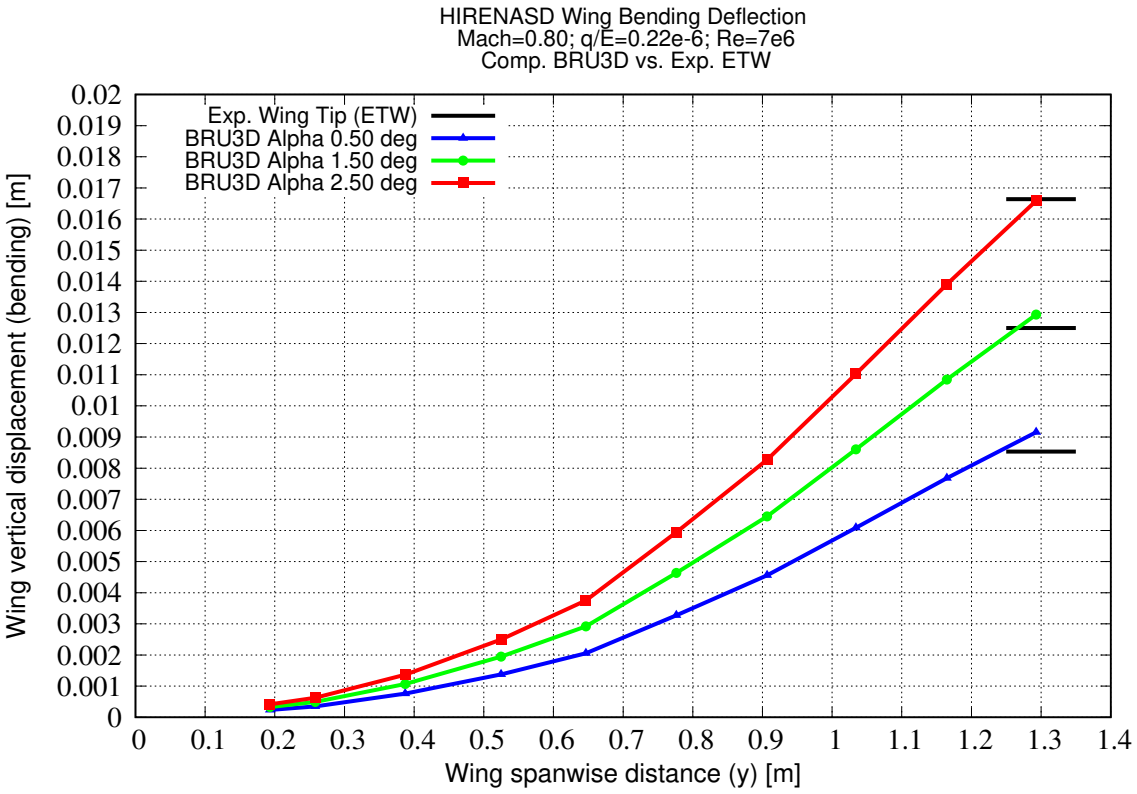

Figure 6 – HIRENASD Wing Bending Deflection.

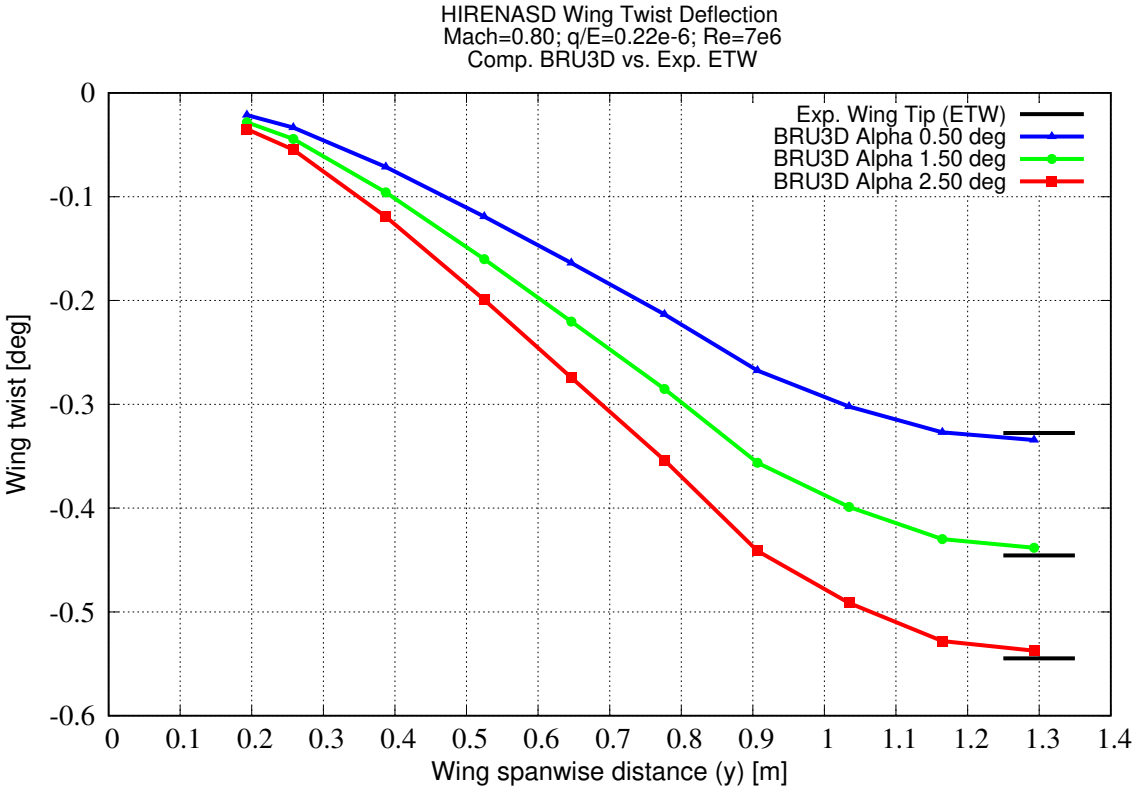

Figure 7 – HIRENASD Wing Twist Deflection.

results when compared to the experimental data. This behavior is true for both rigid configuration and aerostructural calculations. This limitation might be related to the CFD mesh resolution and further aerodynamic grid refinements are probably needed in order to improve the results.

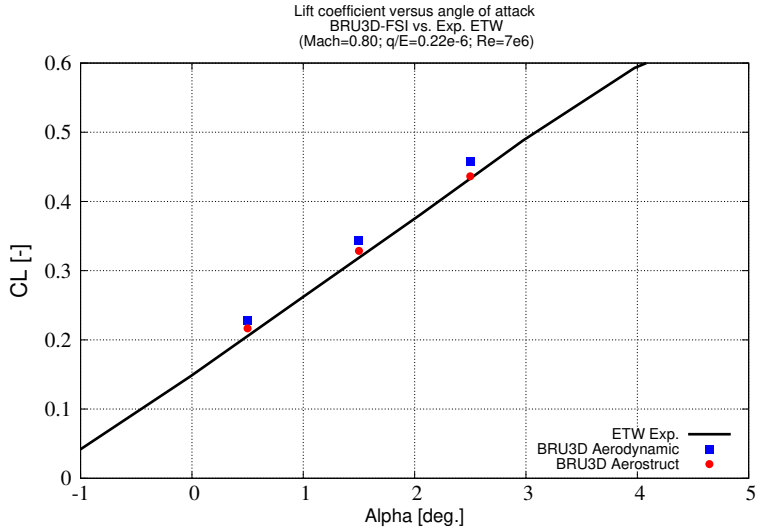

(a) Lift coefficient comparisons.

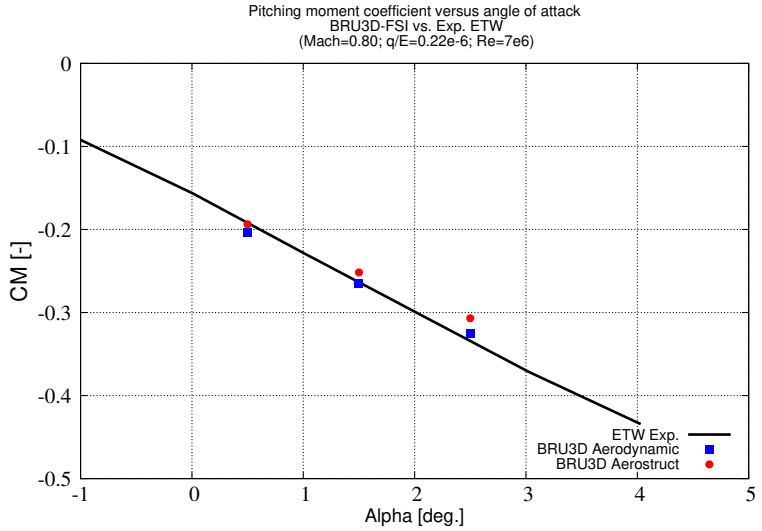

(b) Pitching moment coefficient comparisons.

Figure 8 – HIRENASD aerodynamic coefficients at $M_\infty = 0.80$, $Re = 7 \times 10^6$ and $q/E = 0.22 \times 10^{-6}$.

3.3 Pressure Distribution

As previously described, a typical wing deflection due to positive aerodynamic loads induces a local spanwise wing twist reduction and, as a consequence, the wing loading near the tip is also reduced. These effect are depicted in Fig. 9, where the present purely aerodynamic and aerostructural pressure coefficient contours for the solution over the wing are compared for two different angles of attack. For both flow attitudes, $\alpha = 0.5\ deg$ and $\alpha = 1.5\ deg$, the wing loading is reduced by the inclusion of the aeroelastic effects. The figure shows, in the left hand plots, the purely aerodynamic solution for the rigid wing, whereas the right hand plots present the pressure coefficient contours for the aerostructural simulations. The same color coding is used for all contours.

Figure 9 also superimposes the shear lines over the pressure coefficient contours in order to help the visualization of the flow topology over the wing. It can be observed that, downstream of the shock wave, there is considerable distortion of the shear lines towards the wing tip, indicating that the spanwise flow seems to be intensified by the effects of the shock wave impinging on the boundary layer flow. Nevertheless, there are no relevant changes in shear line directions that can be attributed to the structural flexibility effects. In other words, the overall flow topology is not significantly affected by the inclusion of the wing aeroelastic deformation. Moreover, the figures also indicate that the wing inboard region does not show any relevant changes in aerodynamic loading for the angles of attack considered here, as expected.

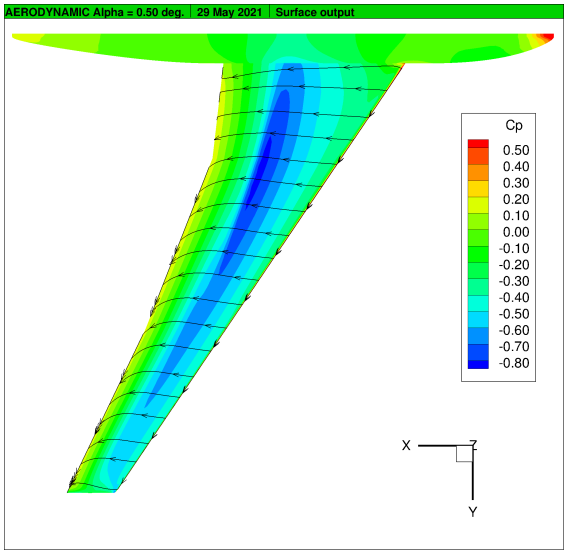

(a) Aerodynamic run, $\alpha = 0.50$ deg.

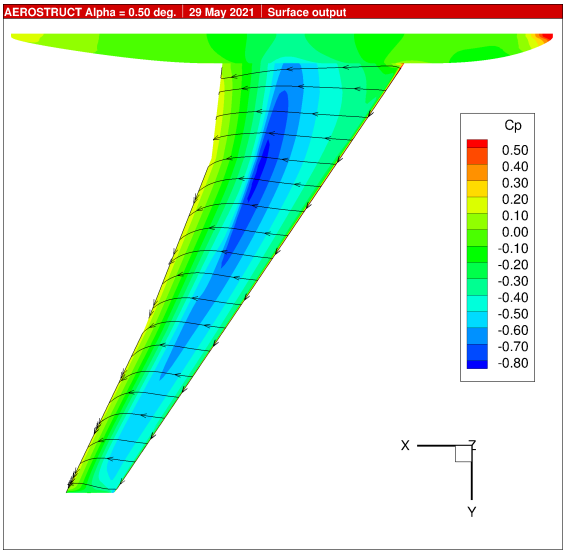

(b) Aerostructural run, $\alpha = 0.50$ deg.

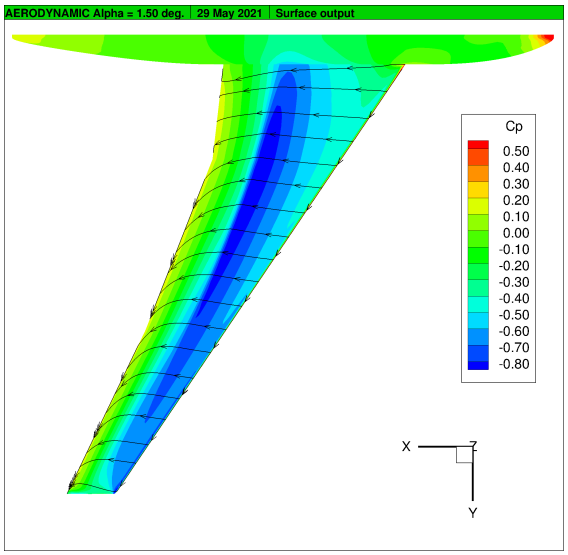

(c) Aerodynamic run, $\alpha = 1.50$ deg.

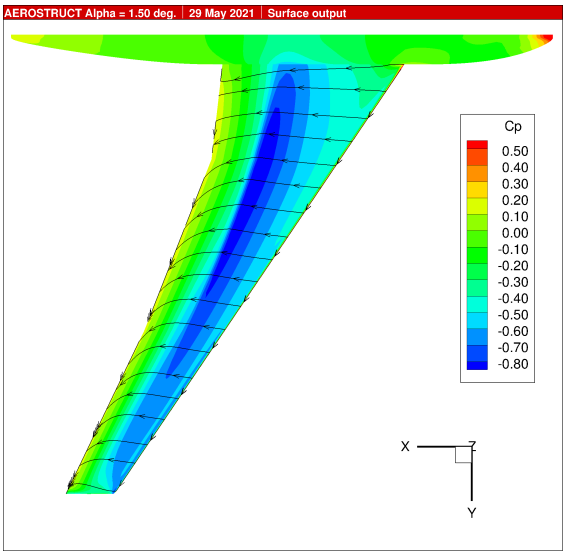

(d) Aerostructural run, $\alpha = 1.50$ deg.

Figure 9 – Comparison of purely aerodynamic and aerostructural pressure coefficient distributions for the HIRENASD model at $M_\infty = 0.80$, $Re = 7 \times 10^6$ and $q/E = 0.22 \times 10^{-6}$.

4. Concluding Remarks

A successful integration between the BRU3D in-house CFD code and a modal-based static structural analysis code was accomplished. Such integration uses the constant strain triangle shape function formulation in order to transfer aerodynamic loads into the structural dynamic surface grid, and it also uses a radial basis function approach in order to transfer the structural deflections back into the aerodynamic grid. The complete process has been described in a reasonable degree of detail in the paper. Due to the large amount of accessible technical information, the HIRENASD model is used in order to evaluate the capability of the present fluid-structure interaction process.

The results obtained in terms of wing deflections show good agreement with experimental ETW data for both wing tip vertical displacement and twist. Moreover, there is also good agreement for the lift coefficient comparisons. On the other hand, the calculated moment coefficient distribution, as a function of angle of attack, has presented some deviations in the curve slope when compared to the experimental data. The effect of wing tip loading relief due to local angle of attack reduction for swept wings is indicated and discussed. Furthermore, pressure coefficient results over the wing are also presented, allowing the visualization of the effects of structural deformation in the aerodynamic loading characteristics of the wing.

Overall, the present results are quite encouraging. They indicate that the developed framework for static aeroelastic analyses is performing appropriately. Clearly, however, additional aerodynamic grid refinement studies are necessary in order to further improve the comparison of the aerodynamics properties calculated for this configuration, when compared to the experimental results. This observation is true for both purely aerodynamic and aerostructural calculations.

5. Acknowledgments

The authors acknowledge the support for the present research provided by Conselho Nacional de Desenvolvimento Científico e Tecnológico, CNPq, under the Research Grants No. 309985/2013-7 and No. 402238/2013-3. The work is also supported by the computational resources from Center for Mathematical Sciences Applied to Industry, CeMEAI, funded by Fundação de Amparo à Pesquisa do Estado de São Paulo, FAPESP, under the Research Grant No. 2013/07375-0. Additional support to the second author under the FAPESP Research Grant No. 2013/07375-0 is also gratefully acknowledged.

6. Contact Author Email Address

Mail to: j.allanantunes@gmail.com
Mail to: joaoluiz.azevedo@gmail.com

7. Copyright Statement

References

[1] Ballmann J, Dafnis A, Braun C, Korsch H, Reimerdes H-G, Olivier H. The HIRENASD Project: High Reynolds Number Aerostructural Dynamics Experiments in the European Transonic Windtunnel (ETW). *25th Congress of the International Council of the Aeronautical Sciences (ICAS)*, 2006, pp. 1041–1050.

[2] Ballmann J, Dafnis A, Korsch H, Buxel C, Reimerdes H-G, Brakhage K-H, Olivier H, Braun, C, Baars A, Boucke A. Experimental Analysis of High Reynolds Number Aero-Structural Dynamics in ETW. *46th AIAA Aerospace Sciences Meeting and Exhibit*, Jan. 2008. https://doi.org/10.2514/6.2008-841

[3] Reimer L, Boucke A, Ballmann J, Behr M. Computational Analysis of High Reynolds Number Aero-Structural Dynamics (HIRENASD) Experiments. *The International Forum on Aeroelasticity and Structural Dynamics*. IFASD Paper No. 2009-130, 2009.

[4] Chwalowski P. Preliminary Computational Analysis of the HIRENASD Configuration in Preparation for the Aeroelastic Prediction Workshop. *The International Forum on Aeroelasticity and Structural Dynamics*. IFASD Paper No. 2011-108, 2011.

[5] AePW-1. *Aeroelastic Prediction Workshop*, 2012. https://c3.nasa.gov/dashlink/static/media/other/AEPW_-legacy.htm.

[6] Chwalowski P, Heeg J, Dalenbring M, Jirasek A, Ritter M, Hansen T. Collaborative HIRENASD Analyses to Eliminate Variations in Computational Results. *IFASD - International Forum on Aeroelasticity and Structural Dynamics*. IFASD-2013-1D, 2013.

[7] Beckert A, Wendland H. Multivariate Interpolation for Fluid-Structure Interaction Problems Using Radial Basis Functions. *Aerospace Science and Technology*, Vol. 5, No. 2, 2001, pp. 125-134. https://doi.org/10.1016/S1270-9638(00)01087-7

[8] de Boer A, van der Schoot M S, Bijl H. New Method for Mesh Moving Based on Radial Basis Function Interpolation. *European Conference on Computational Fluid Dynamics, ECCOMASS CFD*, 2006. https://repository.tudelft.nl/islandora/object/uuid:95e7df53-71d1-49ee-b65c-e52ba8c70a55?collection=research.

[9] Rendall T C S , Allen C B. Efficient Mesh Motion Using Radial Basis Functions with Data Reduction Algorithms. *Journal of Computational Physics*, Vol. 228, No. 17, 2009, pp. 6231–6249. https://doi.org/10.1016/j.jcp.2009.05.013

[10] Rendall T C S, Allen C B. Reduced Surface Point Selection Options for Efficient Mesh Deformation Using Radial Basis Functions. *Journal of Computational Physics*, Vol. 229, No. 8, 2010, pp. 2810–2820. https://doi.org/10.1016/j.jcp.2009.12.006

[11] Kedward L, Allen C B, Rendall T C S. Efficient and Exact Mesh Deformation Using Multiscale RBF Interpolation. *Journal of Computational Physics*, Vol. 345, 2017, pp. 732–751. https://doi.org/10.1016/j.jcp.2017.05.042

[12] Lyrio J, Azevedo J L F, Rade D and da Silva R. Computational Static Aeroelastic Analyses in Transonic Flows. *AIAA Aviation 2020 Forum*, June 2020. https://doi.org/10.2514/6.2020-2718.

[13] Souza F J, Neto A S, Deschamps C J, Azevedo J L F, Bigarella E D V, de Oliveira G L. Implementation and Evaluation of RANS Turbulence Models in the BRU3D Code. *18th ABCM International Congress of Mechanical Engineering – COBEM*, 2005.

[14] Junqueira Junior C, Azevedo J L F, Scalabrin L, Basso E. A Study of Physical and Numerical Effects of Dissipation on Turbulent Flow Simulations. *Journal of Aerospace Technology and Management*, Vol. 5, No. 2, 2013, pp. 145–168. https://doi.org/10.5028/jatm.v5i2.179

[15] da Silva, R G, Azevedo J L F. Numerical Simulations of Turbulent Flows Over the ONERA M6 and DLR F6 Configurations. *30th Congress of the International Council of the Aeronautical Sciences*, ICAS, 2016.

[16] da Silva R G, Azevedo J L F. CFD Investigation of Aerodynamic Coefficients and Stall Characteristics for High Lift Configurations. *31st Congress of the International Council of the Aeronautical Sciences*, ICAS, 2018.

[17] Craig R and Kurdila A. *Fundamentals of Structural Dynamics*. 2nd edition, Wiley, 2006.

[18] CEPID. *Center for Mathematical Sciences Applied to Industry*, http://www.cemeai.icmc.usp.br/index.php.

[19] Guruswamy G. A Review of Numerical Fluids/Structures Interface Methods for Computations Using High-Fidelity Equations. *Computers & Structures* Vol. 80, No. 1, 2002, pp. 31–41. https://doi.org/10.1016/S0045-7949(01)00164-X

[20] Saad Y. *Iterative Methods for Sparse Linear Systems*. 2nd edition, Society for Industrial and Applied Mathematics, 2003.